

# 3D Printing of Ultralight Biomimetic Hierarchical Graphene Materials with Exceptional Stiffness and Resilience

Meiwen Peng, Zhen Wen, Lingjie Xie, Jian Cheng, Zheng Jia, Danli Shi, Huajie Zeng, Bo Zhao, Zhiqiang Liang,\* Teng Li,\* and Lin Jiang\*

Biological materials with hierarchical architectures (e.g., a macroscopic hollow structure and a microscopic cellular structure) offer unique inspiration for designing and manufacturing advanced biomimetic materials with outstanding mechanical performance and low density. Most conventional biomimetic materials only benefit from bioinspired architecture at a single length scale (e.g., microscopic material structure), which largely limits the mechanical performance of the resulting materials. There exists great potential to maximize the mechanical performance of biomimetic materials by leveraging a bioinspired hierarchical structure. An ink-based three-dimensional (3D) printing strategy to manufacture an ultralight biomimetic hierarchical graphene material (BHGMs) with exceptionally high stiffness and resilience is demonstrated. By simultaneously engineering 3D-printed macroscopic hollow structures and constructing an ice-crystal-induced cellular microstructure, BHGMs can achieve ultrahigh elasticity and stability at compressive strains up to 95%. Multiscale finite element analyses indicate that the hierarchical structures of BHGMs effectively reduce the macroscopic strain and transform the microscopic compressive deformation into the rotation and bending of the interconnected graphene flakes. This 3D printing strategy demonstrates the great potential that exists for the assembly of other functional materials into hierarchical cellular structures for various applications where high stiffness and resilience at low density are simultaneously required.

Assembly of lightweight engineering and functional materials with superb mechanical performance, such as high stiffness, super resilience, and stability, is highly demanded to pave ways for their practical applications.<sup>[1]</sup> However, how to simultaneously achieve both stiffness and resilience in a man-made material at low-density remains a challenging scientific and engineering issue. Biological materials have found their way to achieve outstanding mechanical properties at low density by assembling sophisticated hierarchical structures from microscopic to macroscopic scales, and thus provide inspirations for designing and manufacturing advanced biomimetic materials.<sup>[2]</sup> Plant materials, such as plant stem<sup>[3]</sup> and wood,<sup>[4]</sup> represent an important class of lightweight natural materials with superb mechanical properties. The slender grass stems of *Elytrigia repens* is a representative natural material with high mechanical performance and lightweight features owing to a specially evolved hierarchical architecture with a macroscopically hollow and microscopically cellular structure.


The macroscopically hollow structure combined with the cellular microstructure serves as an excellent force-bearing structure that is conducive to the dispersion of strain and stress, and thus efficiently enhances the stiffness, and resilience and reduce the density, simultaneously.<sup>[5]</sup> In recent years, the constructions of biomimetic structures have attracted extensive attention because of their potential ability to achieve high mechanical properties and lightweight artificial engineering and functional materials.<sup>[6]</sup> Despite progresses in the construction of biomimetic structures, the poor mechanical properties at low density remain as a major bottleneck in artificial biomimetic materials, which are mainly due to the lack of appropriate structures at both macro- and microlevels at the same time.

The ink-based 3D printing, as a powerful additive manufacturing technique for producing 3D structures both in microscopic and macroscopic scales,<sup>[6b,7]</sup> shows great potential to assemble materials into 3D hierarchical structures. Additionally, 3D printing displays distinct advantages of high degree of freedom in structure design, which enable the ability to design and construct versatile structures for realizing the

M. W. Peng, Dr. Z. Wen, L. J. Xie, D. L. Shi, H. J. Zeng, B. Zhao, Dr. Z. Q. Liang, Prof. L. Jiang  
Institute of Functional Nano and Soft Materials (FUNSOM)  
Jiangsu Key Laboratory for Carbon-Based Functional Materials & Devices and Joint International Research Laboratory of Carbon-Based Functional Materials and Devices  
Soochow University  
Suzhou 215123, Jiangsu, P. R. China  
E-mail: zqliang@suda.edu.cn; ljjiang@suda.edu.cn

Dr. J. Cheng, Prof. T. Li  
Department of Mechanical Engineering  
University of Maryland College Park  
College Park, MD 20742, USA  
E-mail: lit@umd.edu

Prof. Z. Jia  
Department of Engineering Mechanics  
Zhejiang University  
Hangzhou 310027, P. R. China

 The ORCID identification number(s) for the author(s) of this article can be found under <https://doi.org/10.1002/adma.201902930>.

DOI: 10.1002/adma.201902930

desirable mechanical performances and/or functionalities. In recent years, graphene materials have become a hot research topic because of its unique electronic,<sup>[8]</sup> optical,<sup>[9]</sup> thermal,<sup>[10]</sup> and mechanical properties.<sup>[11]</sup> Assembly of lightweight 3D graphene materials with robust mechanical performance, such as high stiffness, super resilience, and stability, is highly desirable in energy,<sup>[12]</sup> environment,<sup>[13]</sup> engineering,<sup>[14]</sup> and electronics<sup>[15]</sup> applications. On the basis of these demands, several 3D printing methods, including isooctane supported printing,<sup>[16]</sup> cold sink assisted printing,<sup>[17]</sup> and directly printing in air environment,<sup>[12e,18]</sup> have been demonstrated for printing graphene aerogel materials. Compared with the conventional bulk graphene aerogels, 3D-printed graphene materials demonstrated unique properties, such as rapid ions and electrons transportation, which are beneficial for electrochemical performance.<sup>[19]</sup> Importantly, functional dopants can be easily incorporated into the 3D-printed graphene materials, which demonstrates a potential of producing multifunctional graphene-based composites to meet the requirements of diverse applications, such as the high-performance electrodes for energy-related applications.<sup>[12e,18,20]</sup> Additionally, compared with conventional bulk graphene aerogels, 3D-printed graphene materials exhibit enhanced mechanical performance, such as high stiffness and stretchability.<sup>[16,17,21]</sup> However, further enhancement in resilience and stability of 3D-printed graphene materials at ultralow density ( $<10 \text{ mg cm}^{-3}$ ) remains highly demanded for diverse applications in which superelasticity is required (i.e., ultrafast and ultrasensitive pressure sensor, electrochemical electrode, and compressible electronics). The ability to construct 3D graphene materials with biomimetic architectures in both micro and macroscale for achieving excellent mechanical properties at low density is highly desirable yet remains as a significant scientific and engineering challenge.

In this study, inspired by *Elytrigia repens*, we demonstrated an ink-based 3D printing strategy for scalably constructing ultralight 3D biomimetic hierarchical graphene materials (BHGMs) with exceptionally high stiffness and resilience (Figure 1). Multiscale finite element analysis (FEA) calculations reveal the pivotal role of the hierarchical cellular structures in the accommodation of the macro- and microcompressive deformation, which further guide us to print biomimetic hierarchical structured graphene materials to achieve outstanding biomimetic mechanical performance at low density. By optimizing the partially reduced graphene oxide (pr-GO) ink and combining with the freeze casting treatment, the biomimetic hierarchical structure of macroscopically hollow scaffold and microscopically cellular is realized simultaneously. (Figure 1b). The resulting 3D-printed BHGMs exhibit exceptional resilience at an ultralow density of  $8.5 \text{ mg cm}^{-3}$ . It has been demonstrated that the BHGMs can maintain 90.1% after cyclic compression of 95% strain for ten times under the maximum pressure (66 kPa). Additionally, compared with the previous reported conventional bulk graphene materials with comparable density, our 3D-printed BHGMs achieved a threefold enhancement in stiffness (Young's modulus) and can withstand 22 000 times its own weight without deformation. The triboelectric nanogenerators (TEGs) based on these 3D-printed BHGMs as elastically deformable electrode generate large voltages under the low-frequency compressing. In addition, the output voltage

increases as the increase of compression, which indicates that the BHGMs based compressible TENGs can function as an ultralight active pressure sensors. More importantly, our strategy demonstrated in this work successfully realized the 3D printing of biomimetic hierarchical materials and could be extended to handle other functional materials, demonstrating great potential on various applications where high mechanical performance and low density are required simultaneously.

Figure 1a,b schematically illustrates the design philosophy of 3D printing of BHGMs. By optimizing the pr-GO ink, the 3D BHGMs were printed by assembling the filaments layer by layer (Figure 1c). Note that the ink-based 3D printing of BHGMs crucially depends on the development of printable ink with desired rheological properties, which in turn depend on the properties of fillers, solvent and/or binder, and the solid content. In this work, we synthesized large lateral sized GO sheets for preparing 3D printable inks and helping to obtain low-density 3D graphene structure. Atomic force microscopy (AFM) measurement (Figure S1, Supporting Information) reveals the as-synthesized GO sheets with a lateral size larger than  $5 \mu\text{m}$  and a thickness of  $0.8 \text{ nm}$ . GO aqueous dispersions have adjustable rheology, which enable them to work as high-performance ink for various fabrication techniques.<sup>[22]</sup> In addition, the large lateral sized GO sheets are beneficial to achieve higher shear viscosity and storage modulus than the smaller GO sheets in aqueous solution,<sup>[23]</sup> which help obtain printable ink at a relatively low solid content and thus favor printing of low-density graphene structures. We experimentally found that the aqueous-based ink with a solid content of 2.5 wt% is very promising for 3D printing (Figure S2c,d, Supporting Information). More importantly, the pr-GO can form microscopic cellular structure by freeze casting due to the extrusion of the ice crystal during the freezing process.<sup>[24]</sup> Based on the above considerations, we developed 3D printable pr-GO inks using ascorbic acid (AA) aqueous solution and large lateral sized GO sheets suspensions. AA is employed to act as weak reductant to reduce GO to reduced graphene oxide (RGO) with controllable reduction degree. The pr-GO1 inks exhibit high viscosity, significant shear-thinning behavior, and adequate modulus (Figure S2, Supporting Information). The  $G'$  and  $\tau_y$  of pr-GO inks are as large as  $\approx 10^5$  and  $\approx 10^3 \text{ Pa}$ , respectively, which endow the shape retention of extruded ink filaments. Importantly, the cross-linked GO sheets in pr-GO1 ink give it higher apparent viscosity, storage modulus ( $G'$ ) and loss modulus ( $G''$ ) than that of pristine GO ink with the same solid content. As a result, the macrosized hollow structure printed from pr-GO1 ink can maintain their shapes without external support, which provide high flexibility over the printing process, and thus very desirable for the fast manufacture in air (Figure 1c).

Under the extruding force of the ice crystals generated in rapidly freezing process, abundant cellular microstructure will be formed in the 3D-printed pr-GO filaments. After drying and annealing reduction, the cellular microstructure is retained in graphene filaments. Figure S3 (Supporting Information) schematically illustrates the formation of microscopic cellular structure in 3D-printed BHGM using ice crystals as template. In contrast, in the 3D-printed filaments that have not been treated by freeze casting, the GO sheets are densely packed and aligned along the printing direction (Figure S4, Supporting

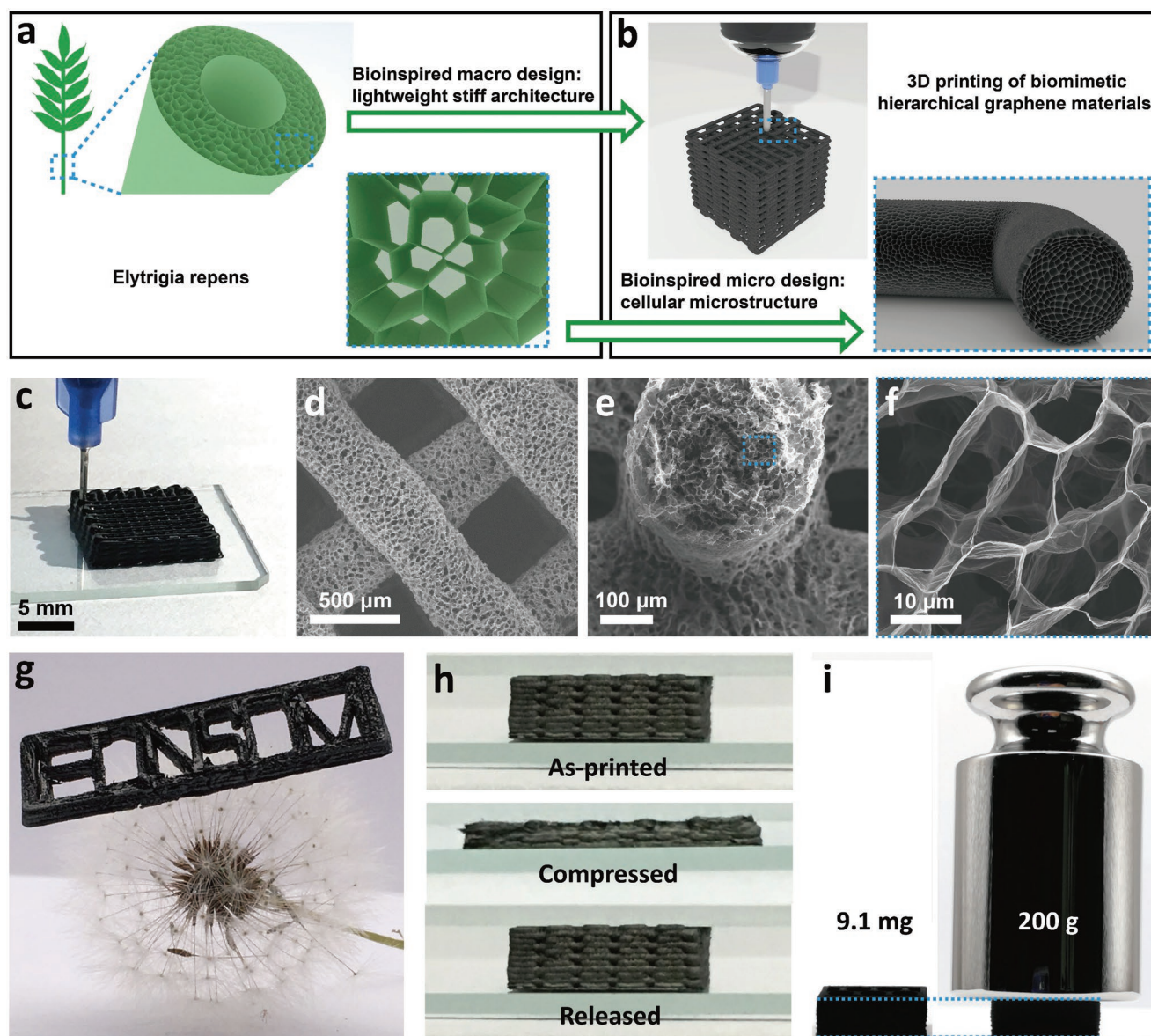


**Figure 1.** *Elytrigia repens* and 3D-printed BHGMs. Schematic illustration of hierarchical structure of a) grass stems of *Elytrigia repens* and b) 3D printing of BHGMs. c) Optical and d–f) SEM images of 3D-printed BHGMs. g) Ultralight, h) superelastic, and i) high stiffness properties exhibition of 3D-printed BHGMs.

Information) due to the shear-stress during the extrusion of GO ink filaments. Note that, for pr-GO inks, the reduction degree of the GO sheets largely affects the microstructure in the printed graphene filaments (Figure S5, Supporting Information), and the subsequent mechanical performance. Figure 1d–f gives the representative scaffold, ink filament, and cellular microstructures printed from the pr-GO1 ink. Figure 1f shows cellular microstructure with an average pore size of around 10  $\mu\text{m}$ . The 3D-printed macroscopic scaffold structure and the cellular microstructure make the 3D-printed BHGMs compressible and have excellent mechanical properties at ultralow density ( $9.3 \text{ mg cm}^{-3}$ ). As shown in Figure 1g, such an ultralight BHGMs can be held up by a dandelion. More importantly, the ultralight BHGMs exhibit superelasticity property as evidenced

by the complete recovery at a 95% deformation (Figure 1h). Surprisingly, these ultralight honeycomb BHGMs can support 22 000 times its own weight without obvious deformation (Figure 1i).

To guide the 3D printing of graphene materials for achieving high comprehensive mechanical performance at low density, multiscale FEA calculations were performed to reveal the effects of the macroscopic scaffold and the microscopic cellular of 3D graphene materials on their mechanical properties. As described in Figure 2a,b, both the hierarchical graphene materials (HGMs) with clutter microstructure and the BHGMs with cellular microstructure were modeled and calculated for comparison. Figure 2d represents the FEA model of the 3D graphene at sub-millimeter scale, which was set based on the macroscopic



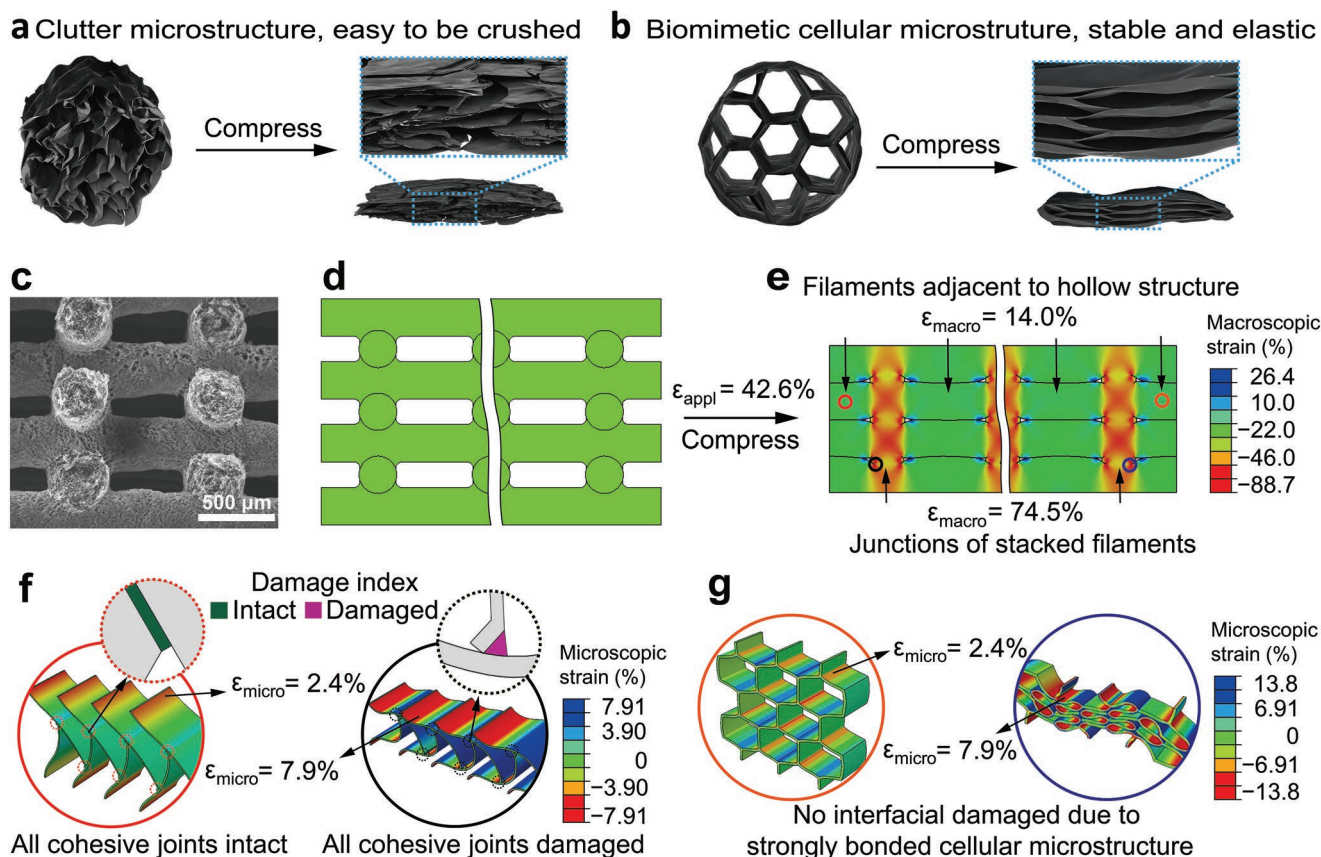


**Figure 2.** Hierarchical breakdown of the deformation and compressive strain from macro to microscopic scale in the 3D-printed graphene structures. Schematically showing the compression of a) the clutter microstructure, and b) the biomimetic cellular microstructure. c) SEM image and d) the corresponding FEA model of the original state of a representative volume element (RVE) of the 3D-printed scaffold of BHGMs and HGMs. e) Macroscopic strain resulting from an applied compression of  $\epsilon_{\text{appl}} = 42.6\%$ . Macroscopic strain concentrates at the junctions of stacked filaments where the highest compressive strain  $\epsilon_{\text{macro}} = 74.5\%$ , while the strain elsewhere in the structure maintains at a lower value  $\epsilon_{\text{macro}} = 14\%$ . f) Deformation of the microscopic graphene flakes at two distinctive locations in the 3D-printed clutter-like HGMs structure where the macroscopic strain equals to (left) 14% and (right) 74.5%. At microscopic level, only weakly interacting bonds populate the graphene joints in HGMs. These bonds are susceptible to damage when deformation is extreme. Insets show the pristine state of the graphene joints at lower macroscopic strain and the damaged joints at higher macroscopic strain. g) Deformation of the constituent graphene flakes at macroscopic strain (left) 14% and (right) 74.5% of 3D-printed BHCMs which have strong bonds formed at graphene joints due to freeze casting. Where  $\epsilon_{\text{macro}} = 74.5\%$ , the maximum microscopic strain is only 13.8%. Where  $\epsilon_{\text{macro}} = 14\%$ , the maximum compressive strain acting on the microscopic graphene flakes equals to 4%. The color contours in (f) and (g) illustrate the microscopic strain experienced by the graphene flakes.

scaffold structure of the 3D-printed graphene material (as shown in Figure 2c). Under an applied compression with thickness reduction of 42.6%, the macroscopic structure deforms to a state illustrated in Figure 2e. Due to the hollow scaffold structure, the compressive load is readily accommodated by the collapse and closure of those macroscopic openings, which in turn largely mitigate the applied deformation: at  $\epsilon_{\text{appl}} = 42.6\%$ , the localized macroscopic strain in filaments adjacent to hollow structure is reduced to 14% (represented by the green part), while an elevated strain (up to 74.5% and shown in red) appearing only at the junctions of the stacked macroscopic material filaments. The deformation sequence of the scaffold is shown in Figure S6 (Supporting Information). The color contour reports the maximum (absolute value) in-plane principal strain.

Next, the localized macroscopic strain is applied to the microscopic structure to evaluate the resulting microscopic strain experienced by the constituent pr-GO flakes. For the HGMs with clutter-like microstructure, the graphene flakes in HGMs

are combined via weakly interacting intermolecular bonds such as van der Waals force (modeled as cohesive zones). Therefore, such a clutter microstructure is susceptible to irreversible interfacial damage at elevated strain levels. When the clutter-like microstructure is compressed, at where macroscopic compressive strain equals to 74.5%, the maximum resultant microscopic strain on the graphene is 7.9%, the relative rotational movement between the adjacent graphene flakes causes the intermolecular joints to damage (Figure 2f). The deformation sequence of the clutter-like microstructure is shown in Figure S7a (Supporting Information). The red circles highlight the failed cohesive joints at the corresponding macrostrain. Figure S7b (Supporting Information) shows the damage state evolution of two representative joints in the structure as a function of prescribed macrostrain. The percentage of damaged joints increases as the macrostrain accumulates, indicating that the damage of the entire structure progresses at elevated deformation (Figure S7c, Supporting Information). Consequential detachment of the



originally bonded graphene flakes leads to a reduction in stiffness of the entire macroscopic HGMs structure. In contrast, the 3D-printed BHGMs are not susceptible to interfacial damage owing to its strongly bonded honeycomb-like cellular microstructure resulting from the freeze casting process (Figure 2b). BHGMs retain elasticity since no damage mechanism is initiated in the microscopic level at localized macrostrain of 74.5% (Figure 2g). The deformation sequence (as shown in Figure S8, Supporting Information) of the BHGMs microstructure shows three distinctive stages during the compression: Figure S8b (Supporting Information) represents the onset of cell wall buckling at localized macroscopic strain 21.5%; Figure S8c (Supporting Information) shows the starting point of cell wall contact at macrostrain 51.6%; and Figure S8d (Supporting Information) shows a fully collapsed microscopic structure at elevated macrostrain 71.0%. Therefore, the supreme elasticity of the BHGMs can be achieved by constructing the unique combination of (1) a 3D-printed macroscopic hollow structure which effectively mitigates the localized strain and (2) a strongly bonded microscopic cellular structure which sustains extreme compressive deformation.

By simultaneously engineering the 3D-printed macroscopic structures and the ice crystals induced cellular microstructure, similar to the structure of the stems of *Elytorgia repens*, ultralight 3D BHGMs were obtained. As a comparison, the 3D HGMs with disorderly stacked graphene sheets were also fabricated and characterized. In theory, graphene sheets inside the 3D HGMs randomly stacked together would result in a small space for deformation and poor compressive properties (Figure 3a,b). In contrast, the cross-sectional scanning electron microscopy (SEM) images (Figure 3d,e) show the interconnected cellular microstructure of 3D BHGMs, which provide an adequate space for accommodating larger deformation, and the continuous graphene walls can effectively rebound after being compressed, providing superior stability. After different degrees of compression, it can be seen from the stress-strain curves that the 3D BHGM can fully recover (Figure 3f) but the 3D HGM cannot fully recover to the precompression state after 95% strain (Figure 3c). Figure S9 (Supporting Information) shows the 90% compressive stress-strain curves of 3D-printed HGM and BHGM for the first 100 cycles. The maximum pressure and Young's modulus of 3D BHGM remained at 82.7% and 53.7% of the initial value after 90% cyclic compression for 100 cycles, but the 3D HGM only remained 2.0% and 2.2% of the initial value (Figure 3g,h). By comparison, BHGM exhibits better cycle stability than HGM, and the Young's modulus of BHGM is also much higher than that of HGM, indicating that the initial deformation of BHGM requires more pressure and it is stiffer than HGM. The reason why the Young's modulus of BHGM is higher is that the inner graphene walls are obviously thicker than HGMs (Figure S10, Supporting Information). After 95% cyclic compression for ten cycles, the maximum pressure and Young's modulus of 3D BHGM remained at 90.1% and 73.3% of the initial value, and irreversible deformation is only 0.9% (Figure S11, Supporting Information). Figure 3i shows the Young's modulus of 3D-printed BHGMs is more than three times higher than the traditional superelastic bulk graphene materials.<sup>[25]</sup> In addition, the resilience and stability of our ultralight BHGMs are also remarkably better than the

previously reported 3D-printed graphene materials (Table S1, Supporting Information).<sup>[16–18,26–28]</sup>

Microstructure of the BHGMs can be effectively controlled by changing the proportion of GO and AA in the pr-GO ink, ultimately affecting the compression performance. At the same stirring time and GO concentration, when the mass ratio of AA and GO is 0.5 (BHGM-0.5), there will be some large pores inside the material, but the graphene walls are discontinuous and very cluttered (Figure S12a, Supporting Information). As the mass ratio of AA and GO increases to 1 (BHGM), continuous graphene cellular structure is formed (Figure S12b, Supporting Information). When the mass of AA is twice the amount of GO (BHGM-2), as the degree of reaction between AA and GO increases, the cellular structure becomes denser (Figure S12c, Supporting Information). The compression performance of BHGM-0.5, BHGM, and BHGM-2 is shown in Figure S12d–i (Supporting Information). After ten cycles, the irreversible deformation of BHGM is minimal, indicating that its structure is the most stable (inset images of Figure S12d–f, Supporting Information). Since the graphene walls of BHGM-0.5 are discontinuous and cluttered, the max stress, Young's modulus, and energy loss coefficient of BHGM-0.5 are less than BHGM and BHGM-2, indicating its poor compression performance (Figure S12g–i, Supporting Information). Max stress of BHGM-2 is higher than BHGM because of its dense microstructure, but the max stress of cycle 10 is 83.7% of cycle 1, which is less than 90.1% of BHGM (Figure S12g, Supporting Information). The Young's modulus of BHGM of cycle 10 is 73.3% of cycle 1, which is bigger than 51.7% of BHGM-2 (Figure S12h, Supporting Information). The energy loss coefficient of cycle 10 to cycle 1 of BHGM and BHGM-2 is 88.5 and 83.0%, indicating BHGM is more stable (Figure S12i, Supporting Information). In conclusion, BHGM is more stable and stronger than BHGM-0.5 and BHGM-2.

In addition to the microstructure, we also experimentally investigated the effects of the macroscopic geometry of 3D-printed BHGMs on their mechanical properties. Compared to the BHGM scaffold with cross-stacked construction (Figure S13a–c, Supporting Information), the hexagonal honeycomb BHGM with layered construction (Figure S13d–f, Supporting Information) exhibits a little more stable than the scaffold structure at 50% compression strain (Figure S14, Supporting Information). After ten cycles of 50% compression the layered honeycomb structure deformed by 0.7% and the cross-stacked scaffold structure deformed by 1.5%. We suggest that the more sufficiently contacted between the upper and lower filaments in honeycombs endows more uniform macro- and microstrain, and thus with smaller stress concentration and structural damages. As a result, the honeycombs exhibit better compression performance than that of the scaffolds under the same compression.

The 3D-printed BHGMs have a significantly lower resistance when compressed and maintain good resistance stability during multiple cycles of compression (Figure S15, Supporting Information), which makes it a promising compressible electrode material. Video S1 (Supporting Information) shows that the 3D-printed BHGM can be used as a piezoresistive LED light switch. The larger the pressing deformation, the brighter the LED light. After several quick presses, the 3D-printed BHGM is still intact, indicating its high stability.

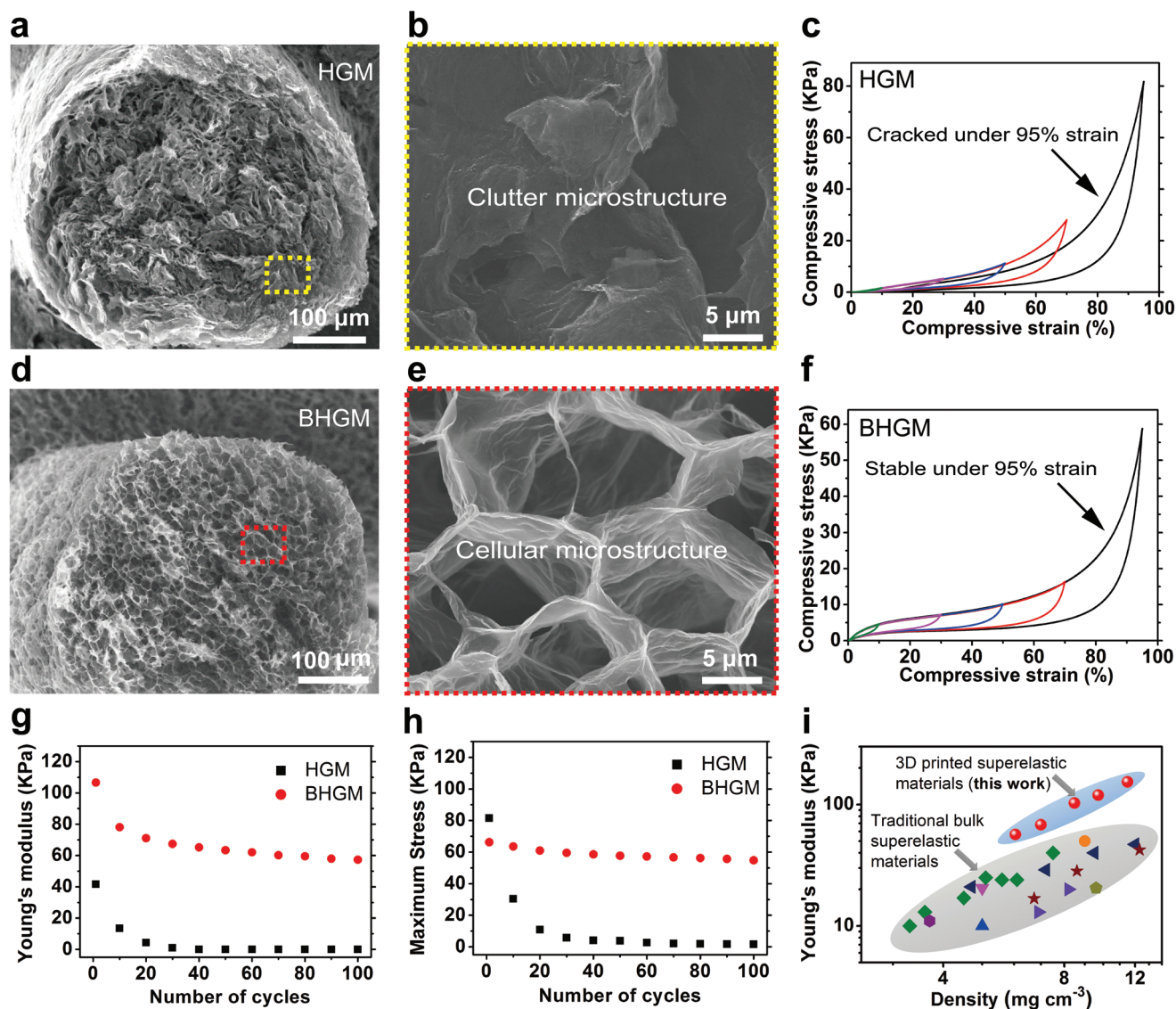


**Figure 3.** A comparison of the structures and the compressive performances between 3D-printed HGMs and BHGMs. SEM images of a,b) clutter microstructure of HGM and d,e) cellular microstructure of BHGM. Stress–strain curves of c) HGM and f) BHGM at different compressive strains. Note that the HGM cracked at 95% compression, while BHGM remains stable. g) Young's modulus and h) maximum stresses at 90% strain of HGM and BHGM during the first 100 compression cycles. The density of 3D HGM and 3D BHGM is 8.7 and 8.5  $\text{mg cm}^{-3}$ , respectively. i) Young's modulus of 3D-printed BHGMs show threefold higher than the conventional bulk superelastic materials with comparable geometric density.<sup>[25]</sup>

The harvesting, storage, and utilization of energy are becoming a worldwide issue due to the growing energy needs. The TENG based on coupling effects of triboelectrification and electrostatic induction could convert mechanical energy into electricity, which provides a new energy harvesting approach.<sup>[29]</sup> In view of the fascinating advantages of ultralight, superelastic, and high stability, BHGMs as electrode and fluorinated ethylene propylene (FEP) as triboelectric layer formed the bottom part, another Al foil is laminated on the finished structure to achieve the contact-separation mode TENG as shown in Figure 4a. Figure 4b shows a representative TENG with BHGMs electrode. Figure 4c presents the electricity generating mechanism of the contact-separation mode TENG based on BHGMs electrode. In the initial state, there is no charge generated and no electrical

potential between two electrodes. When Al foil contacts with the FEP film, because of their difference in electron affinity, the negative triboelectric charges would remain on the FEP film and reserve the positive charges on the Al foil. Note that the generated negative triboelectric charges will be retained on the FEP surface for a long period.<sup>[30]</sup> When removing external forces, positive charges will be induced in the 3D-printed BHGMs electrode, and the electrons will transport from the 3D-printed BHGMs electrode to Al foil under the short-circuit condition due to electrostatic effect. When the pressure is repressing, the distance between the two layers becomes smaller, which causes the electron flow back in the reverse direction due to electrostatic induction. When the two layers are recontacted, all induced charges are neutralized. The output performance of

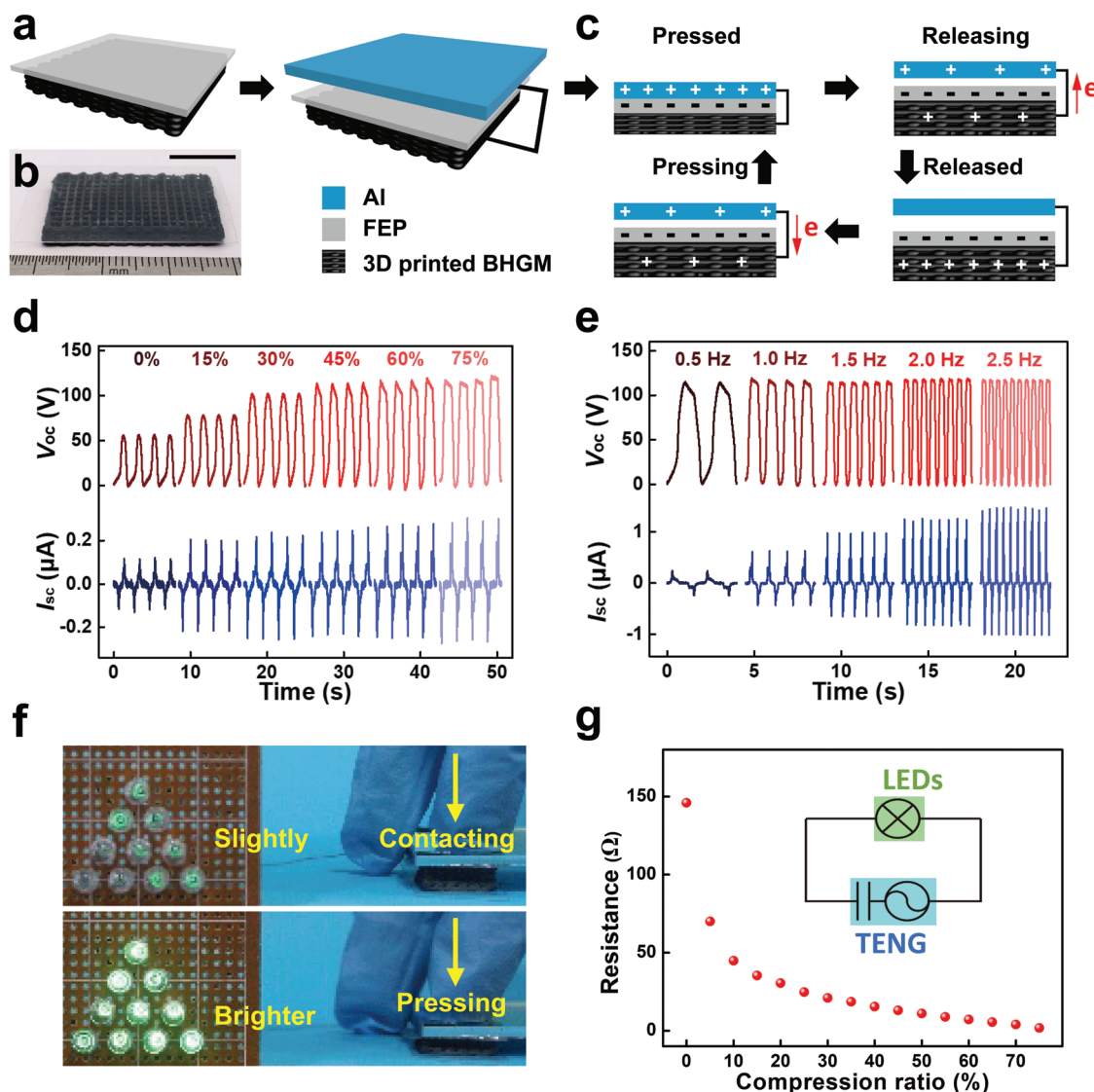


**Figure 4.** 3D-printed BHGMs as compressible electrode in TENG. a) Structure schematic of the TENG based on the 3D-printed BHGM electrode. b) Optical image of a representative TENG with the 3D-printed BHGMs electrode (scale bar: 1 cm). c) Schematic illustration of the working mechanism of the electricity generation under short-circuit conditions at contact-separation mode. d)  $V_{OC}$  and  $I_{SC}$  of the TENG under various compression ratio ranging from 0 to 75%. e)  $V_{OC}$  and  $I_{SC}$  of the TENG under various motion frequencies ranging from 0.5 to 2.5 Hz. f) Photographs of the ten green LEDs lighted up by hand tapping at less compression (top) and at large compression (bottom). g) Dependence of the resistance of the 3D-printed BHGMs electrode under different compression ratio. Inset is the circuit diagram.

the TENG is evaluated by a cyclic movement through a linear motor. In order to investigate the influence of the compression ratio on the electrical outputs, the TENG is measured at 0.5 Hz frequency, which is contacted by an Al foil with an area of  $2 \times 3 \text{ cm}^2$ . In the open-circuit condition, as the external pressure is withdrawn, the open-circuit voltage ( $V_{OC}$ ) will increase corresponding to the vertical gap distance between the two layers ( $d$ ) as shown in the following equation

$$V_{oc} = \frac{\sigma \times d}{\epsilon_0} \quad (1)$$

$$V_{oc,0} - V_{oc} = \frac{\sigma \times (d_0 - d)}{\epsilon_0} \quad (2)$$

where  $\epsilon_0$  is the permittivity in vacuum and  $\sigma$  is the triboelectric charge density, which is considered as constant in this work. It should be noted that the  $V_{oc}$  starts decreasing when the external pressure is applied and reverts to its maximum level  $V_{oc,0}$  when the pressure is fully removed ( $d = d_0$ ). Since the FEP structure is not completely flat which has microstructure, when the compression is small (0 to 45%), the gap distance ( $d$ ) cannot be completely pressed to its minimum value, which voltage difference rise from 56.3 to 117.6 V. When the amount of compression reaches 45%, the  $d$  reaches its minimum value under a large pressure, so the voltage remains unchanged. Meanwhile, with the increase of the compression ratio from 0 to 75%, the short-circuit current ( $I_{SC}$ ) rises from 0.12 to 0.29  $\mu\text{A}$ . It worth noting that the  $I_{SC}$  rises rapidly when the compression ratio increases



from 0 to 30%. In contrast, the  $I_{SC}$  rises slightly by further increasing the compression ratio from 30 to 75% (Figure 4d). This is because of that the  $I_{SC}$  is mainly determined by the different conductivity of the 3D-printed BHGMs electrode, which is due to degrees of the compression of the electrode. Figure 4e exhibits the test results of  $V_{OC}$  and  $I_{SC}$  for the TENG under various working frequencies (from 0.5 to 2.5 Hz) at 75% compression ratio. No obvious output changes can be observed in the  $V_{OC}$  ( $\approx 114.5$  V) under different frequencies, while the peak value of the  $I_{SC}$  increases with raising the working frequency from 0.23  $\mu$ A at 0.5 Hz to 1.48  $\mu$ A at 2.5 Hz.

In addition, with the increase of the compression ratio, the resistance of the 3D-printed BHGMs electrode is 146  $\Omega$  at the beginning of the uncompressed to 1.7  $\Omega$  at 75% compression, as shown in Figure 4g. When manually tapping the TENG can sufficiently light up ten LEDs in series, which has higher brightness at high compression ratio than low compression due to increased output power with the increasing of compression degree (Figure 4f, Video S2, Supporting Information). On the basis of this characteristic, we suggest that this compressible TENG can function as an active pressure sensor, in which the pressure can be monitored by the output electrical signal generated under different degrees of compression. To confirm this concept, we measured the output voltage of the compressible TENGs as a function of the applied pressure and time, respectively (Figure S16, Supporting Information). It can be found that the TENG sensor can respond to the applied pressure ranging from 24 to 1200 Pa (Figure S16a,b, Supporting Information). In addition, the response time is as short as 80 ms under the applied pressure of 24 Pa (Figure S16d, Supporting Information). Importantly, this sensor can monitor the applied pressure without the need for external power supply.

In summary, we demonstrated an ink-based 3D printing of BHGMs based on pr-GO ink. The significant enhancement in mechanical properties finds its origin in the biomimetic hierarchical structure, which were proved by both experiments and simulations. This ink-based 3D printing strategy has diverse advantages: (i) compatible with fast and large-scale fabrication due to the controllable and flexible printing process; (ii) BHGMs from microscale to macroscale are obtained; (iii) macroscopic geometry and size are easily controllable by adjusting the printing program. 3D graphene architected materials with a biomimetic hierarchical structure have great potential and opportunities for many applications when ultralight, superelastic, and high stable properties are required. As an example, based on the compression-induced resistance changes and superelastic property, the BHGMs were first demonstrated to serve as the compressible electrodes in high-performance TENG. More importantly, the 3D printing and freeze casting strategy developed in this work has great potential and opportunities for assembling materials into 3D biomimetic hierarchical structures. The biomimetic hierarchical structures of functional nanomaterials enable superb mechanical properties at a low density and thus hold promise in a wide range of potential applications.

## Supporting Information

Supporting Information is available from the Wiley Online Library or from the author.

## Acknowledgements

M.W.P., Z.W., and L.J.X. contributed equally to this work. This work was financially supported by National Key R&D Program of China (International Collaboration program) granted by Chinese Ministry of Science and Technology (2016YFE0129800). This is also a project supported by the National Natural Science Foundation of China (21822202, 61804103) and the Natural Science Foundation of Jiangsu Province (BK20150007). This is a project funded by 111 project, Collaborative Innovation Center of Suzhou Nano Science & Technology, and the Priority Academic Program Development of Jiangsu Higher Education Institutions (PAPD).

## Conflict of Interest

The authors declare no conflict of interest.

## Keywords

3D printing, biomimetic materials, graphene, triboelectric nanogenerators

Received: May 7, 2019

Revised: June 10, 2019

Published online:

- [1] a) B. Wicklein, A. Kocjan, G. Salazar-Alvarez, F. Carosio, G. Camino, M. Antonietti, L. Bergstrom, *Nat. Nanotechnol.* **2015**, *10*, 277; b) X. L. Zhang, V. A. Oberg, J. Du, J. H. Liua, E. M. J. Johansson, *Energy Environ. Sci.* **2018**, *11*, 354; c) L. Liu, Y. X. Yin, J. Y. Li, S. H. Wang, Y. G. Guo, L. J. Wan, *Adv. Mater.* **2018**, *30*, 1706216; d) M. Karl, J. M. E. Glackin, M. Schubert, N. M. Kronenberg, G. A. Turnbull, I. D. W. Samuel, M. C. Gather, *Nat. Commun.* **2018**, *9*, 1525; e) G. Zhou, E. Paek, G. S. Hwang, A. Manthiram, *Nat. Commun.* **2015**, *6*, 7760; f) B. G. Compton, J. A. Lewis, *Adv. Mater.* **2014**, *26*, 5930; g) M. Kaltenbrunner, T. Sekitani, J. Reeder, T. Yokota, K. Kuribara, T. Tokuhara, M. Drack, R. Schwodiauer, I. Graz, S. Bauer-Gogonea, S. Bauer, T. Someya, *Nature* **2013**, *499*, 458.
- [2] M. A. Meyers, P.-Y. Chen, A. Y.-M. Lin, Y. Seki, *Prog. Mater. Sci.* **2008**, *53*, 1.
- [3] L. J. Gibson, M. F. Ashby, *Cellular Solids: Structure and Properties*, 2nd ed., Cambridge University Press, Cambridge **1997**.
- [4] K. Ando, H. Onda, *J. Wood Sci.* **1999**, *45*, 120.
- [5] G. N. Karam, L. J. Gibson, *Mater. Sci. Eng., C* **1994**, *2*, 113.
- [6] a) L. B. Mao, H. L. Gao, H. B. Yao, L. Liu, H. Colfen, G. Liu, S. M. Chen, S. K. Li, Y. X. Yan, Y. Y. Liu, S. H. Yu, *Science* **2016**, *354*, 107; b) U. G. Wegst, H. Bai, E. Saiz, A. P. Tomsia, R. O. Ritchie, *Nat. Mater.* **2015**, *14*, 23; c) N. Song, Y. Zhang, Z. Gao, X. Li, *Nano Lett.* **2018**, *18*, 5812; d) N. Mittal, F. Ansari, V. K. Gowda, C. Brouzet, P. Chen, P. T. Larsson, S. V. Roth, F. Lundell, L. Wagberg, N. A. Kotov, L. D. Soderberg, *ACS Nano* **2018**, *12*, 6378; e) G. X. Gu, M. Takaffoli, M. J. Buehler, *Adv. Mater.* **2017**, *29*, 1700060; f) C. Zhang, D. A. McAdams II, J. C. Grunlan, *Adv. Mater.* **2016**, *28*, 6292; g) D. Jang, L. R. Meza, F. Greer, J. R. Greer, *Nat. Mater.* **2013**, *12*, 893; h) T. A. Schaedler, A. J. Jacobsen, A. Torrents, A. E. Sorensen, J. Lian, J. R. Greer, L. Valdevit, W. B. Carter, *Science* **2011**, *334*, 962.
- [7] a) E. Shukrun, I. Cooperstein, S. Magdassi, *Adv. Sci.* **2018**, *5*, 1800061; b) D. K. Patel, B.-E. Cohen, L. Etgar, S. Magdassi, *Mater. Horiz.* **2018**, *5*, 708; c) M. Schaffner, J. A. Faber, L. Pianegonda, P. A. Ruhs, F. Coulter, A. R. Studart, *Nat. Commun.* **2018**, *9*, 878;

- d) J. Mueller, J. R. Raney, K. Shea, J. A. Lewis, *Adv. Mater.* **2018**, *30*, 1705001; e) D. Kokkinis, F. Bouville, A. R. Studart, *Adv. Mater.* **2018**, *30*, 1705808; f) S. Gantenbein, K. Masania, W. Woigk, J. P. W. Sesse, T. A. Tervoort, A. R. Studart, *Nature* **2018**, *561*, 226; g) J. T. Muth, P. G. Dixon, L. Woish, L. J. Gibson, J. A. Lewis, *Proc. Natl. Acad. Sci. USA* **2017**, *114*, 1832; h) Z. Liu, D. Qi, W. R. Leow, J. Yu, M. Xiloyannis, L. Cappello, Y. Liu, B. Zhu, Y. Jiang, G. Chen, L. Masia, B. Liedberg, X. Chen, *Adv. Mater.* **2018**, *30*, 1707285; i) H. Yang, W. R. Leow, T. Wang, J. Wang, J. Yu, K. He, D. Qi, C. Wan, X. Chen, *Adv. Mater.* **2017**, *29*, 1701627.
- [8] K. S. Novoselov, A. K. Geim, S. V. Morozov, D. Jiang, Y. Zhang, S. V. Dubonos, I. V. Grigorieva, A. A. Firsov, *Science* **2004**, *306*, 666.
- [9] T. Mueller, F. N. A. Xia, P. Avouris, *Nat. Photonics* **2010**, *4*, 297.
- [10] A. A. Balandin, *Nano Lett.* **2008**, *8*, 902.
- [11] J. W. Suk, R. D. Piner, J. H. An, R. S. Ruoff, *ACS Nano* **2010**, *4*, 6557.
- [12] a) C. Chen, Y. Yang, X. Tang, R. Qiu, S. Wang, G. Cao, M. Zhang, *Small* **2019**, *15*, 1804740; b) X. Zhao, W. Cai, Y. Yang, X. Song, Z. Neale, H. Wang, J. Sui, G. Cao, *Nano Energy* **2018**, *47*, 224; c) C. Zhu, T. Y. Liu, F. Qian, T. Y. J. Han, E. B. Duoss, J. D. Kuntz, C. M. Spadaccini, M. A. Worsley, Y. Li, *Nano Lett.* **2016**, *16*, 3448; d) H. Bi, T. Lin, F. Xu, Y. Tang, Z. Liu, F. Huang, *Nano Lett.* **2016**, *16*, 349; e) S. D. Lacey, D. J. Kirsch, Y. Li, J. T. Morgenstern, B. C. Zarket, Y. Yao, J. Dai, L. Q. Garcia, B. Liu, T. Gao, S. Xu, S. R. Raghavan, J. W. Connell, Y. Lin, L. Hu, *Adv. Mater.* **2018**, *30*, 1705651.
- [13] a) Q. Zhang, F. Zhang, X. Xu, C. Zhou, D. Lin, *ACS Nano* **2018**, *12*, 1096; b) N. Chen, Q. M. Pan, *ACS Nano* **2013**, *7*, 6875.
- [14] a) M. Yang, N. Zhao, Y. Cui, W. Gao, Q. Zhao, C. Gao, H. Bai, T. Xie, *ACS Nano* **2017**, *11*, 6817; b) Q. Song, F. Ye, X. W. Yin, W. Li, H. J. Li, Y. S. Liu, K. Z. Li, K. Y. Xie, X. H. Li, Q. G. Fu, L. F. Cheng, L. T. Zhang, B. Q. Wei, *Adv. Mater.* **2017**, *29*, 1701583.
- [15] a) L. Qiu, B. Huang, Z. He, Y. Wang, Z. Tian, J. Z. Liu, K. Wang, J. Song, T. R. Gengenbach, D. Li, *Adv. Mater.* **2017**, *29*, 1701553; b) Y. Ma, Y. Yue, H. Zhang, F. Cheng, W. Zhao, J. Rao, S. Luo, J. Wang, X. Jiang, Z. Liu, N. Liu, Y. Gao, *ACS Nano* **2018**, *12*, 3209.
- [16] C. Zhu, T. Y. Han, E. B. Duoss, A. M. Golobic, J. D. Kuntz, C. M. Spadaccini, M. A. Worsley, *Nat. Commun.* **2015**, *6*, 6962.
- [17] Q. Zhang, F. Zhang, S. P. Medarametla, H. Li, C. Zhou, D. Lin, *Small* **2016**, *12*, 1702.
- [18] a) X. W. Tang, C. L. Zhu, D. D. Cheng, H. Zhou, X. H. Liu, P. W. Xie, Q. B. Zhao, D. Zhang, T. X. Fan, *Adv. Funct. Mater.* **2018**, *28*, 1805057; b) X. Tang, H. Zhou, Z. Cai, D. Cheng, P. He, P. Xie, D. Zhang, T. Fan, *ACS Nano* **2018**, *12*, 3502.
- [19] a) T. T. Gao, Z. Zhou, J. Y. Yu, J. Zhao, G. L. Wang, D. X. Cao, B. Ding, Y. J. Li, *Adv. Energy Mater.* **2019**, *9*, 1802578; b) B. Yao, S. Chandrasekaran, J. Zhang, W. Xiao, F. Qian, C. Zhu, E. B. Duoss, C. M. Spadaccini, M. A. Worsley, Y. Li, *Joule* **2019**, *3*, 459.
- [20] K. Fu, Y. Yao, J. Dai, L. Hu, *Adv. Mater.* **2017**, *29*, 1603486.
- [21] F. Guo, Y. Jiang, Z. Xu, Y. Xiao, B. Fang, Y. Liu, W. Gao, P. Zhao, H. Wang, C. Gao, *Nat. Commun.* **2018**, *9*, 881.
- [22] S. Naficy, R. Jalili, S. H. Aboutalebi, R. A. Gorkin, K. Konstantinov, P. C. Innis, G. M. Spinks, P. Poulin, G. G. Wallace, *Mater. Horiz.* **2014**, *1*, 326.
- [23] L. Dong, J. Yang, M. Chhowalla, K. P. Loh, *Chem. Soc. Rev.* **2017**, *46*, 7306.
- [24] Y. Shao, M. F. El-Kady, C. W. Lin, G. Zhu, K. L. Marsh, J. Y. Hwang, Q. Zhang, Y. Li, H. Wang, R. B. Kaner, *Adv. Mater.* **2016**, *28*, 6719.
- [25] a) Z. L. Yu, B. Qin, Z. Y. Ma, J. Huang, S. C. Li, H. Y. Zhao, H. Li, Y. B. Zhu, H. A. Wu, S. H. Yu, *Adv. Mater.* **2019**, *31*, 1900651; b) Y. Si, X. Wang, L. Dou, J. Yu, B. Ding, *Sci. Adv.* **2018**, *4*, eaas8925; c) L. Su, H. Wang, M. Niu, X. Fan, M. Ma, Z. Shi, S. W. Guo, *ACS Nano* **2018**, *12*, 3103; d) C. W. Li, D. G. Jiang, H. Liang, B. B. Huo, C. Y. Liu, W. R. Yang, J. Q. Liu, *Adv. Funct. Mater.* **2018**, *28*, 1704674; e) Q. Zhang, D. Lin, B. Deng, X. Xu, Q. Nian, S. Jin, K. D. Leedy, H. Li, G. J. Cheng, *Adv. Mater.* **2017**, *29*, 1605506; f) Y. Wu, N. Yi, L. Huang, T. Zhang, S. Fang, H. Chang, N. Li, J. Oh, J. A. Lee, M. Kozlov, A. C. Chipara, H. Terrones, P. Xiao, G. Long, Y. Huang, F. Zhang, L. Zhang, X. Lepro, C. Haines, M. D. Lima, N. P. Lopez, L. P. Rajukumar, A. L. Elias, S. Feng, S. J. Kim, N. T. Narayanan, P. M. Ajayan, M. Terrones, A. Aliev, P. Chu, Z. Zhang, R. H. Baughman, Y. Chen, *Nat. Commun.* **2015**, *6*, 6141; g) X. Xu, H. Li, Q. Q. Zhang, H. Hu, Z. B. Zhao, J. H. Li, J. Y. Li, Y. Qiao, Y. Gogotsi, *ACS Nano* **2015**, *9*, 3969; h) Y. Si, J. Yu, X. Tang, J. Ge, B. Ding, *Nat. Commun.* **2014**, *5*, 5802; i) Y. Li, J. Chen, L. Huang, C. Li, J. D. Hong, G. Shi, *Adv. Mater.* **2014**, *26*, 4789.
- [26] Y. Q. Jiang, Z. Xu, T. Q. Huang, Y. J. Liu, F. Guo, J. B. Xi, W. W. Gao, C. Gao, *Adv. Funct. Mater.* **2018**, *28*, 1707024.
- [27] D. X. Luong, A. K. Subramanian, G. A. L. Silva, J. Yoon, S. Cofer, K. Yang, P. S. Owuor, T. Wang, Z. Wang, J. Lou, P. M. Ajayan, J. M. Tour, *Adv. Mater.* **2018**, *30*, 1707416.
- [28] R. M. Hensleigh, H. Cui, J. S. Oakdale, J. C. Ye, P. G. Campbell, E. B. Duoss, C. M. Spadaccini, X. Zheng, M. A. Worsley, *Mater. Horiz.* **2018**, *5*, 1035.
- [29] Z. L. Wang, *ACS Nano* **2013**, *7*, 9533.
- [30] L. Lin, Y. N. Xie, S. M. Niu, S. H. Wang, P. K. Yang, Z. L. Wang, *ACS Nano* **2015**, *9*, 922.

# ADVANCED MATERIALS

## Supporting Information

for *Adv. Mater.*, DOI: 10.1002/adma.201902930

### 3D Printing of Ultralight Biomimetic Hierarchical Graphene Materials with Exceptional Stiffness and Resilience

*Meiwen Peng, Zhen Wen, Lingjie Xie, Jian Cheng, Zheng Jia, Danli Shi, Huajie Zeng, Bo Zhao, Zhiqiang Liang,\* Teng Li,\* and Lin Jiang\**



## Supporting Information

### 3D Printing of Ultralight Biomimetic Hierarchical Graphene Materials with Exceptional Stiffness and Resilience

*Meiwen Peng, Zhen Wen, Lingjie Xie, Jian Cheng, Zheng Jia, Danli Shi, Huajie Zeng, Bo Zhao, Zhiqiang Liang,\* , Teng Li,\* and Lin Jiang,\**

#### Experimental Section

**Materials.** Graphite flake was purchased from XFNANO Inc (XF049, 50 mesh).

Concentrated H<sub>2</sub>SO<sub>4</sub> (98 %) and fuming nitric acid were purchased from Chinasun Specialty Products Co., Ltd. and used as received. KMnO<sub>4</sub>, P<sub>2</sub>O<sub>5</sub>, H<sub>2</sub>O<sub>2</sub> (30 %) solution, K<sub>2</sub>S<sub>2</sub>O<sub>8</sub> were purchased from Sinopharm Chemical Reagent Co., Ltd. and used as received. Ascorbic acid (AA) was purchased from Sigma Aldrich.

**Ink Preparation.** Monolayer GO aqueous solution contain GO nanosheets with lateral dimensions larger than 5 µm (Figure S1, Supporting Information) was synthesized according to the previous report.<sup>[1]</sup> GO powder was produced after freeze drying and grinding. GO suspensions with different concentration were prepared by mixing GO powder into D.I. water using a planetary centrifugal mixer (Thinky, GR-8). Partially reduced GO (pr-GO) inks were prepared by mixing AA aqueous solution into GO suspensions at the mass ratio of 0.5 (pr-GO0.5), 1 (pr-GO1), 2 (pr-GO2) of AA and GO.

**3D printing.** 3D printing was performed by a 3D printer modified from an industrial robotic dispenser (Fisnar F5200n) with capability for programmable patterning in 3D structures. In our experiments, a 3D printing nozzle (diameter 400 µm) was used with pressure controlled at 80-200 KPa and the nozzle's moving speed was 4–20 mm/s. The target patterns were printed onto glass wafers in air at room temperature. After printing, the printed architectures were placed in a liquid nitrogen bath for 0.5 h. The architectures were freeze-drying and further

reduction at 80 °C oven for 2h, and then soaked in deionized water for 24 hours to remove soluble impurities. After the second freeze-drying process, the samples were thermally reduced at 1050 °C for 100 min to obtaining 3D printed BHGM. 3D printed BHGM-0.5, BHGM, BHGM-2 were fabricated by using pr-GO0.5, pr-GO1 and pr-GO2 inks under the same preparation condition. 3D printed HGM use GO aqueous suspension as ink under the same printing program and condition.

**FEA modeling of the macroscopic 3D printed HGM/BHGM structure.** The finite element analysis of the macroscopic HGM/BHGM structure is implemented in commercial package ABAQUS. As shown in Fig. 4a, b, the model exhibits a layered structure of solidified HGM/BHGM filaments. The diameter of the filaments is 400 μm which are arranged in parallel with a spacing of 800 μm, and the distance between each layer is 300 μm. The calculation is based on first-order plane strain elements CPE4RH provided by ABAQUS. Due to its high porosity, in macroscopic level the HGM/BHGM is model as a hyper-foam type hyperelastic material. The strain energy density function of the hyper-foam takes the form:

$$W = \sum_i^N \frac{2\mu_i}{\alpha_i^2} \{ \lambda_1^{\alpha_i} + \lambda_2^{\alpha_i} + \lambda_3^{\alpha_i} - 3 + \beta_i^{-1} [J^{-\alpha_i \beta_i} - 1] \} \quad (3)$$

Where  $\lambda_1, \lambda_2, \lambda_3$  are the principal stretches, and  $J$  is the volumetric ratio.  $N, \mu_i, \alpha_i, \beta_i$  are material parameters. The uniaxial compressive behavior of HGM/BHGM is fitted by a two-term hyperfoam material law, i.e.,  $N=2, \mu_1=0.9955\mu_0, \alpha_1=3.4 \times 10^{-4}, \beta_1=0, \mu_2=0.9955\mu_0, \alpha_2=3.71, \beta_2=0$ . Note that the initial shear modulus of the material  $\mu_0$  is related to the fitted parameters via  $\mu_0 = \mu_1 + \mu_2$ . The fitted material constitutive model is valid to represent the compressive behavior of cellular material which is characterized by a plateau and a stiffening regime in the stress-strain curve.

**FEA modeling of the microscopic structure of HGM.** The representative microscopic structure of HGM is modeled as a clutter of graphene flakes. The clutter is formed by two groups of constituent flakes joining at joints. Flakes belong to the same group are in parallel.

Each flake is connected to two other flakes from the other group and the angle between the connected flakes is 60 degree. At the joints where the flakes meet, there exist a thin layer (1 nm in thickness) of cohesive elements COH2D4 to simulate the weakly interacting bonds formed between the flakes. The traction separation constitutive relation of these cohesive elements is defined by an initial stiffness of  $K=0.04E_0/t_c$  in both normal and tangential directions; the damage initiation criterion is determined by a threshold strain  $\varepsilon^{max}=0.2$  in both normal and tangential directions; and the damage evolution is set by a fracture energy  $G_{CI}=10J/m^2$  in the normal direction and  $G_{CII}=100J/m^2$  in the tangential direction. The multiaxial damage evolution is governed by an energy-based second-order power law relation.

**FEA modeling of the microscopic structure of BHGM.** The microscopic structure of BHGM is modeled as honeycomb-like hexagonal cells with their cell wall dimension  $l$  being 10  $\mu m$  and thickness  $t=0.5 \mu m$ . The material model of the graphene flakes is assumed to be elastic with Poisson's ratio 0.3. The outer vertices of the peripheral hexagons are connected to the ground through spring elements to simulate the lateral confinement from the adjacent repetitive cells. The stiffness of the spring is estimated to be  $5 \times 10^{-3} E_0 l/t$ , where  $E_0$  is the Young's modulus of the graphene flake. The color contour reports the max (absolute value) in-plane principal strain.

**Characterizations.** Rheological properties of the inks were characterized using a stress-controlled Rheometer (Kinexus pro, Malvern) with a 40-mm-flat plate geometry and a gap of 1 mm. The compressive characteristics were measured using a universal testing machine (Instron 3365). The surface morphology, and cross-sectional images of the 3D printed BHGMs were investigated by a Zeiss scanning electron microscope (SEM) and a FEI Tecnai F20 transmission electron microscope (TEM). The electrical output measurement of the TENG devices based on 3D BHGMs electrodes were tested by an external tapping force, which was set up by a commercial linear mechanical motor (Winnemotor,



WMUC512075-06-X) with aluminum film, and a programmable electrometer (Keithley model 6514) to obtain the open circuit voltage ( $V_{oc}$ ), short-circuit current ( $I_{sc}$ ) and short-circuit electric quantity ( $Q_{sc}$ ). In the quantitative test, the copper wire, which was attached on the TENG, was connected with the one terminal of a Keithley 6514, and the other terminal of Keithley 6514 was connected to the aluminum film to form the testing circuit.

**Preparation of 3D BHGMs electrode based TENG.** The base and curing agent of the PDMS (10:1, weight ratio) was mixed in a beaker. The 0.2 mL PDMS mixture was injected on the FEP film. Then, put the 3D BHGMs on the PDMS followed by heating at 60 °C for 2 hours to solidify PDMS and bond the FEP film with 3D BHGMs electrode. A copper lead wire was attached on one side of the 3D BHGMs for electrical connection.

### Supplementary Figures

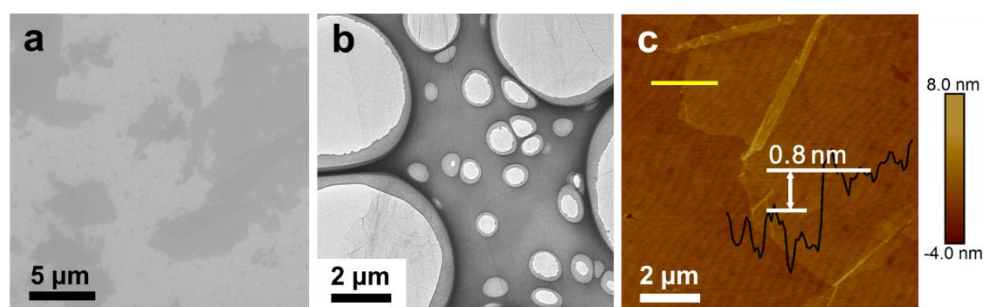


**Figure S1** SEM, TEM and AFM images of the monolayer GO sheet with lateral size larger than 5  $\mu\text{m}$ .

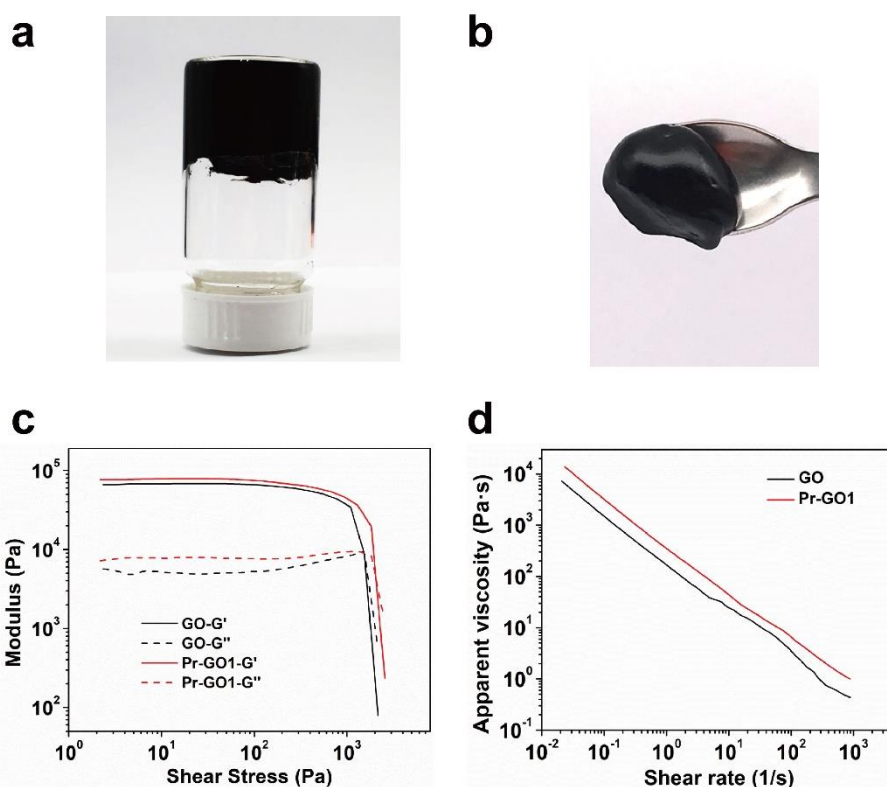


**Figure S2.** **a, b** Pr-GO ink with high viscosity. **c** Storage modulus,  $G'$ , and loss modulus,  $G''$ , as a function of shear stress for GO and pr-GO1 inks. **d** Apparent viscosity as a function of shear rate for pure GO and pr-GO1 inks.

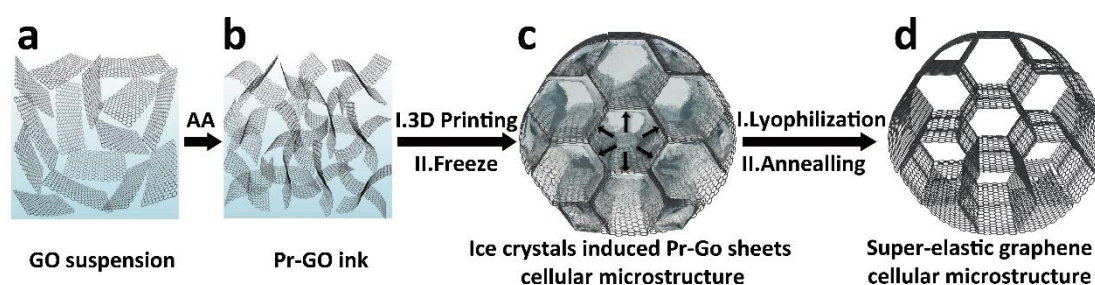


**Figure S3.** Schematic diagram of the formation of microscopic cellular structure. Using pr-GO ink, the printed materials can obtain microscopic cellular structure with ice as template during freeze casting process. The graphene cellular microstructure is super-elasticity after annealing.

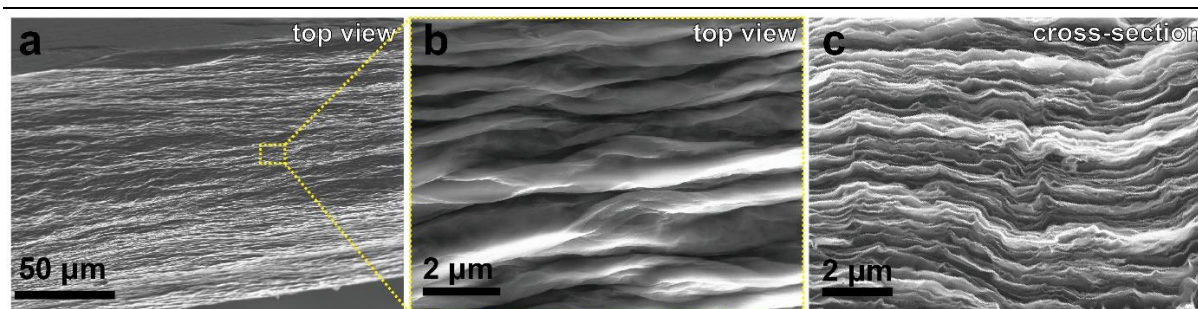


**Figure S4.** SEM images of the 3D printed GO filaments without performing freeze casting treatment.

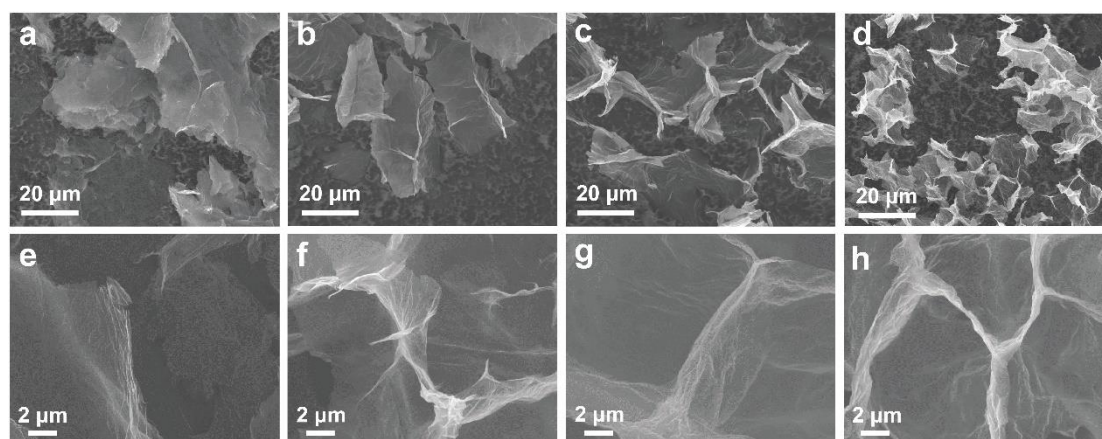


**Figure S5.** SEM images of GO sheets (**a, e**) of GO aqueous suspension and pr-GO microgels of pr-GO0.5 (**b, f**), pr-GO1 (**c, g**) and pr-GO2 (**d, h**) inks after freeze-dry. As the increased amount of AA, the cross-linking degree of GO becomes larger and the pores gradually form and become smaller.

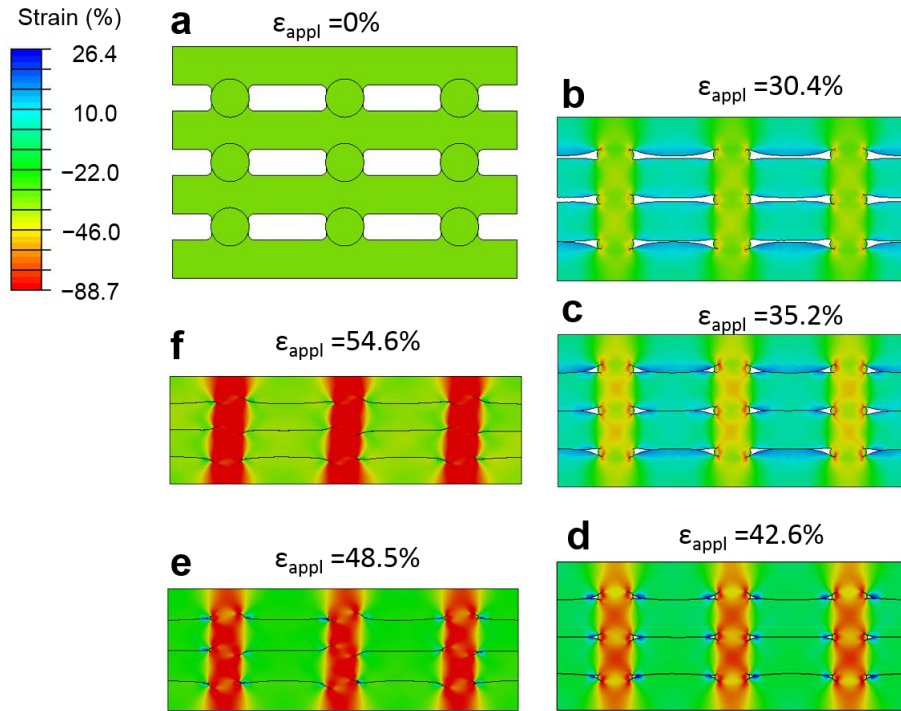


**Figure S6.** Deformation sequence of 3D printed microlattice up to 54.6% thickness reduction (from up left counter-clockwise applied compressive strain increases).

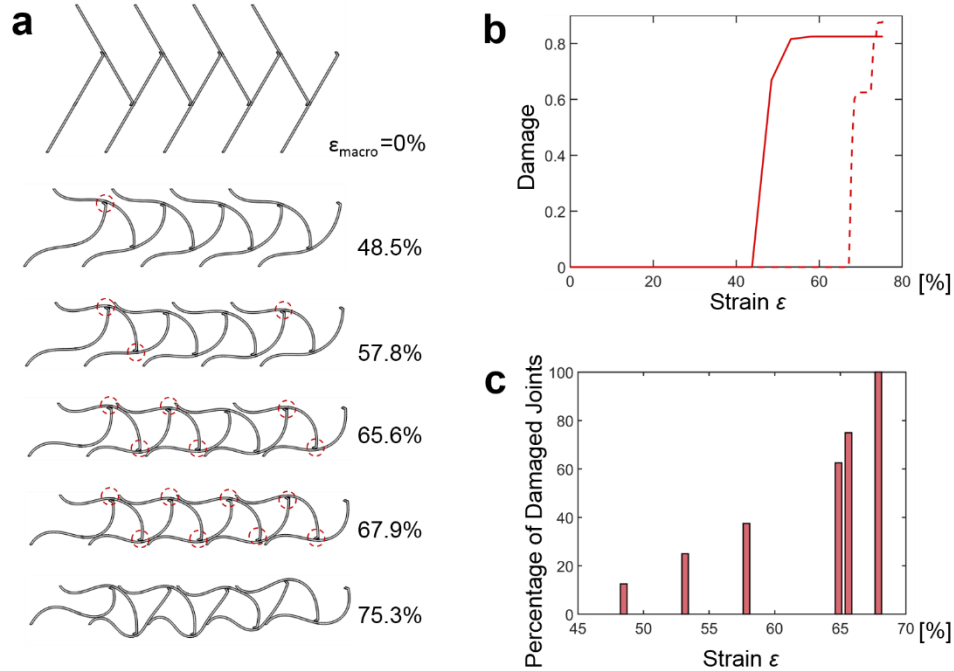


**Figure S7. a** The deformation sequence of clutter microstructure of GM. Red circles highlight the failed joints at the corresponding prescribed macrostrain. **b** The damage state of two joints as a function of strain. **c** Percentage of damaged joints at applied strain (as for a total number of 8 cohesive joints in the model).

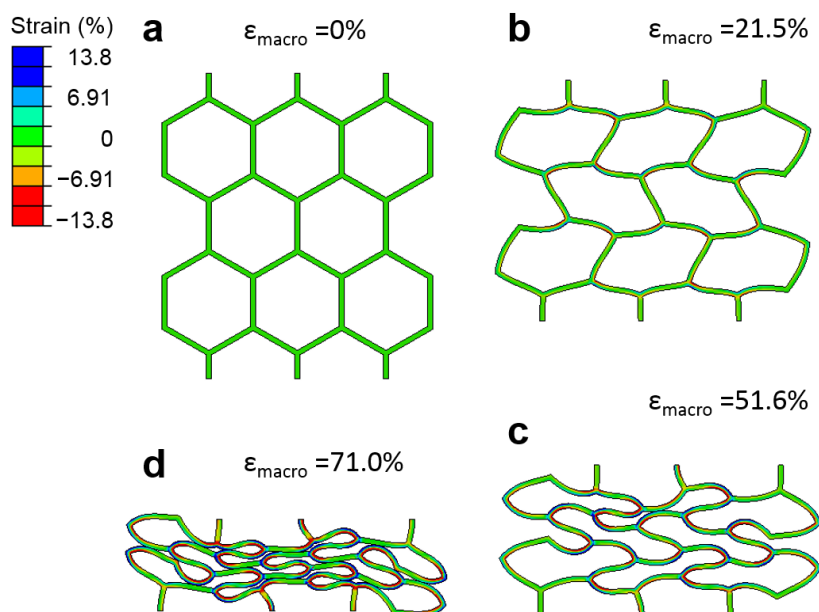


**Figure S8.** Deformation sequence of 3D printed BHGM microscopic structure up to 71.0% thickness reduction (from up left counter-clockwise applied compressive strain. increases).

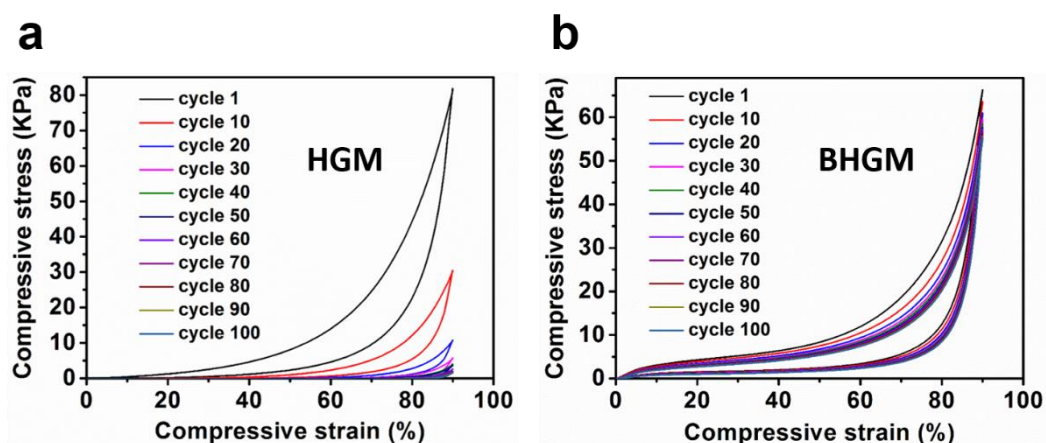


**Figure S9.** The compressive stress–strain curves of 3D printed (a) HGM and (b) BHGM for 100 cycles at compression strain of 90%. The densities of HGM and BHGM are  $8.7 \text{ mg cm}^{-3}$  and  $8.5 \text{ mg cm}^{-3}$ , respectively.



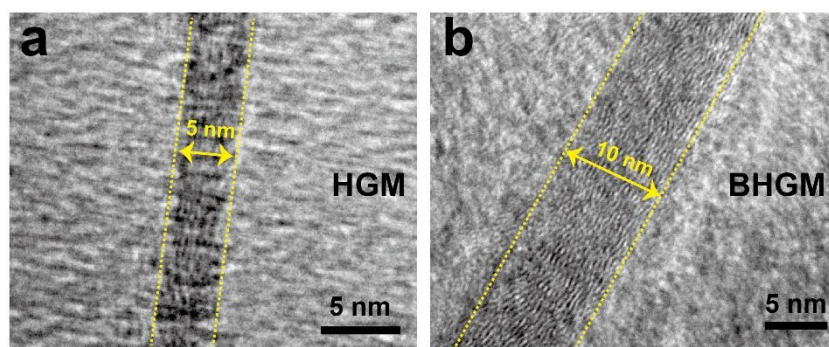


**Figure S10.** TEM images of the graphene sheets within the 3D printed (a) HGM and (b)

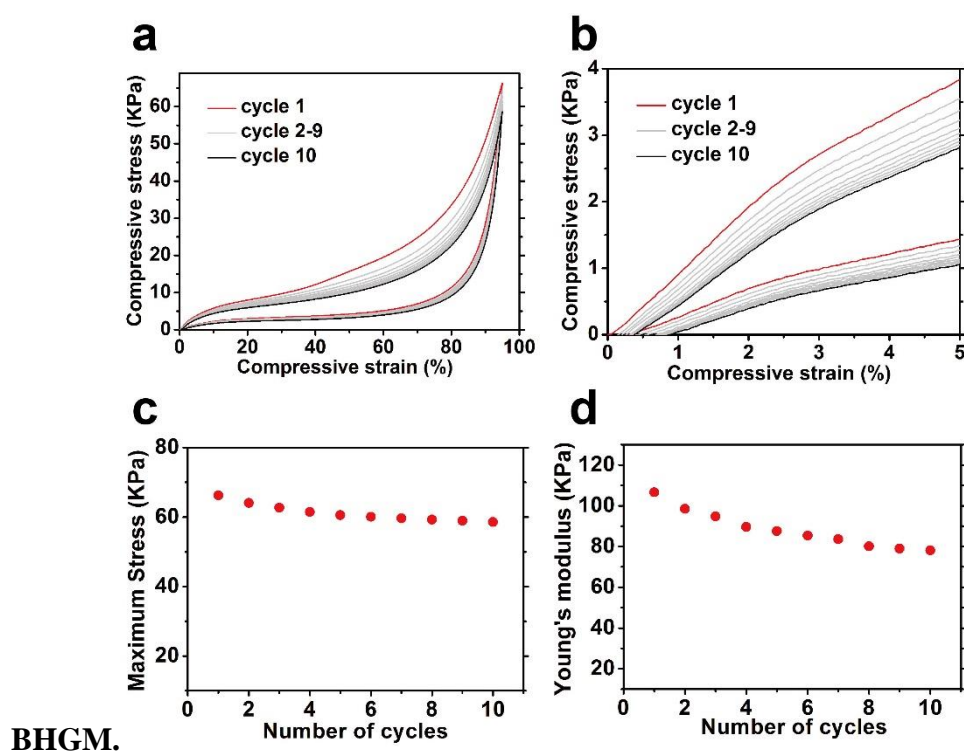


**Figure S11.** Compressive stress–strain curves of 3D printed BHGM-1 for 10 cycles. **a** 95% stress–strain curve of 3D printed BHGM of 10 cycles. **b** Partial enlargement of **a**. **c-d** Young's modulus and maximum stress of 10 cycles. The density of 3D printed BHGM is 8.5 mg/cm<sup>3</sup>.

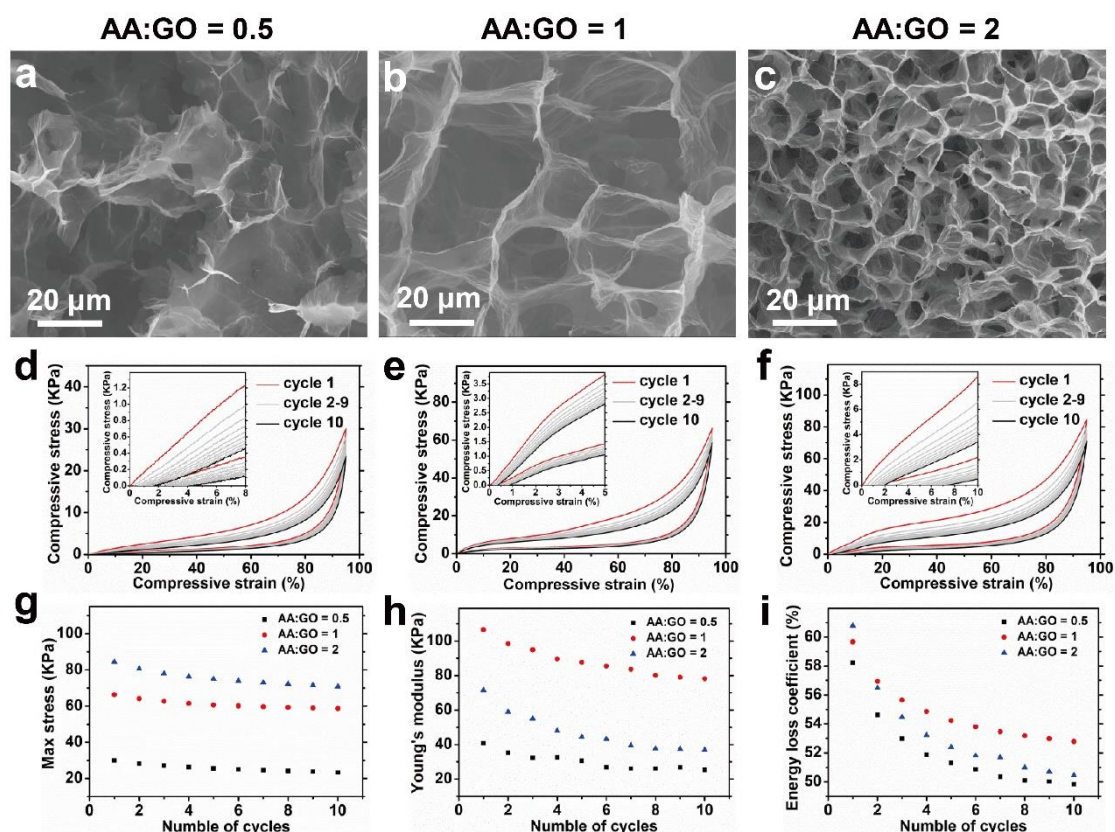


**Figure S12.** Comparison of structure and corresponding compressive performance of 3D printed BHGM-0.5, BHGM and BHGM-2 fabricated using pr-GO inks with the ratio of AA and GO as 0.5 (**a, d**), 1 (**b, e**) and 2 (**c, f**). (**g-i**) Cycle stability of samples fabricated with different pr-GO inks. The density of samples is  $8.5\text{mg/cm}^3$ .

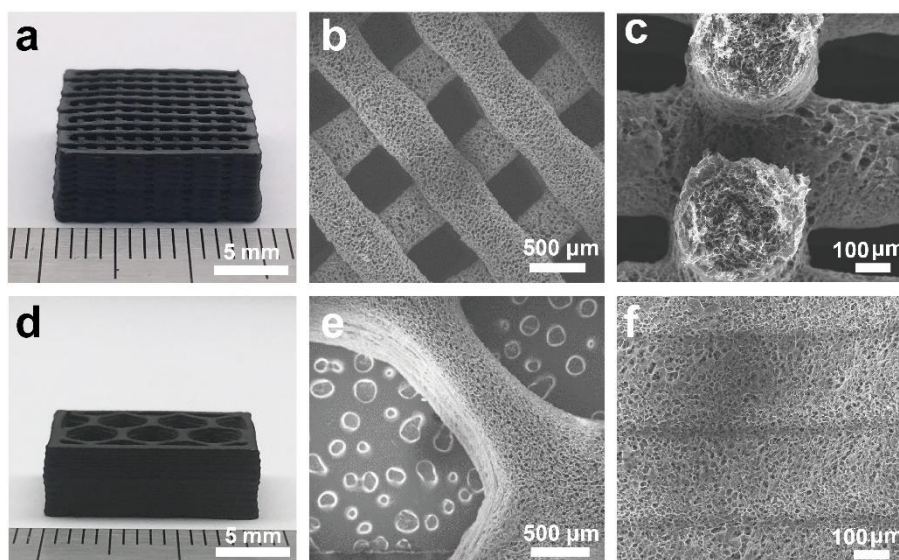


**Figure S13.** a-c Structure characterization of 3D printed microlattice. Optical image (a), SEM images of surface (b) and cross-section (c) of microlattice. d-f Structure characterization of 3D printed honeycomb. Optical image (d), SEM images of surface (e) and cross-section (f) of honeycomb.

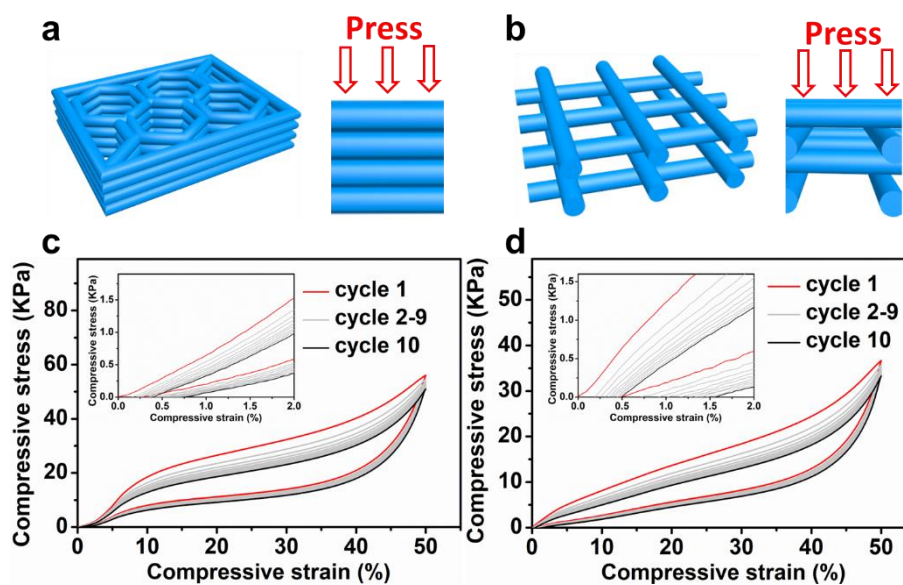


**Figure S14.** Compressive performance of 3D printed BHGMs with honeycomb (a, c) and microlattice (b, d) structure. The density of 3D printed BHGMs is  $8.5 \text{ mg/cm}^3$ .

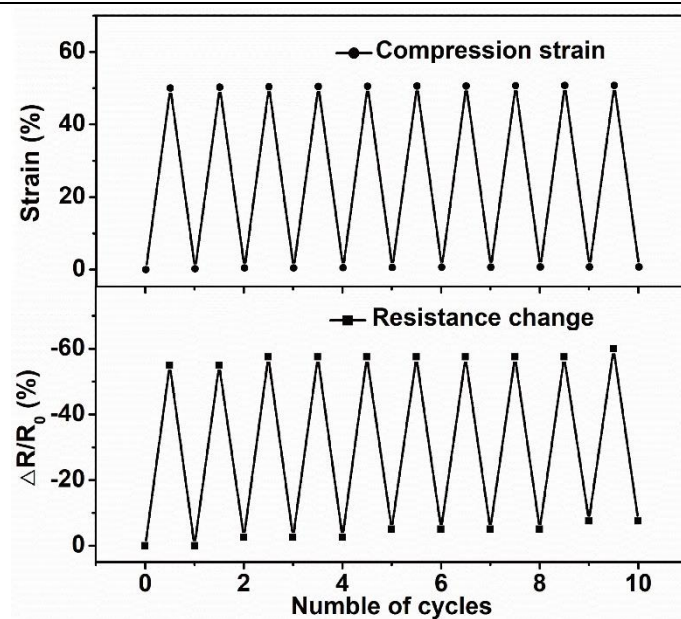


**Figure S15.** Electrical resistance change when repeatedly compressed up to 50% for 10 cycles.



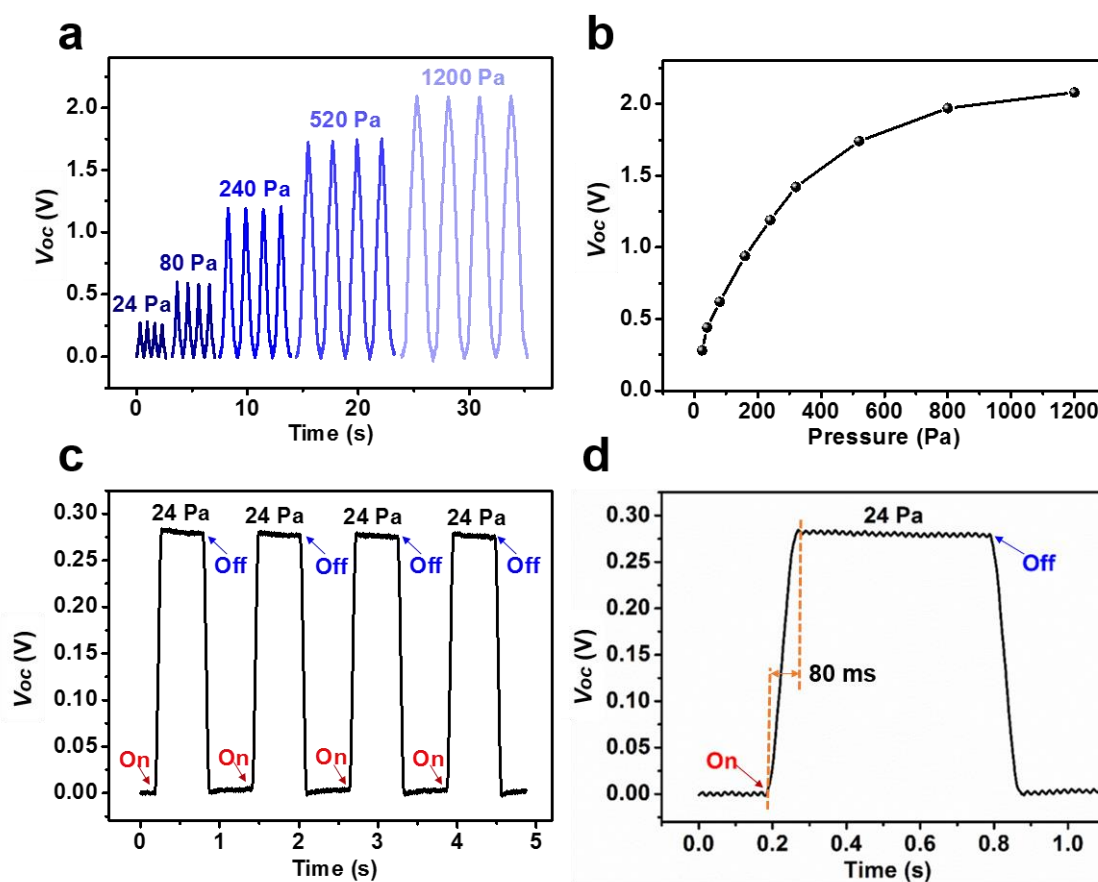


**Figure S16.** 3D BHGM based compressible TENGs as an active pressure sensor. (a, b) Output voltage of the compressible TENGs under different pressure. (c, d) On-Off curve of voltage output under 24 Pa.

**Table S1.** A non-exhaustive survey of 3D printed graphene materials and their key mechanical performances.

Ink Precursor	Density [mg cm <sup>-3</sup> ]	Compressive strain [%]	Maximum pressure retention [%]	References
<b>GO + AA</b>	<b>8.5</b>	<b>95</b>	<b>10 cycles, 90.1</b>	<b>This work</b>
GO + Urea	47	30	5 cycles, 95	<i>ACS Nano</i> 2018 <sup>[18b]</sup>
GO + CaCl <sub>2</sub>	10	80	10 cycles, 75.3	<i>Adv. Funct. Mater.</i> 2018 <sup>[28]</sup>
GO + SA + NCOH	75	/	/	<i>Adv. Funct. Mater.</i> 2018 <sup>[18a]</sup>
Laser-induced graphene	36	10	10 cycles, 80	<i>Adv. Mater.</i> 2018 <sup>[29]</sup>
GO + resin	43.8	/	/	<i>Mater. Horiz.</i> 2018 <sup>[30]</sup>
GO	10	50	10 cycles, 70.6	<i>Small</i> 2016 <sup>[17]</sup>
GO + Silica	53	50	10 cycles, 37.5	<i>Nat. Commun.</i> 2015 <sup>[16]</sup>

**Video S1.** Control switch of LED light with excellent stability.

**Video S2.** 3D printed BHGM as compressible electrode for TENG.

#### References

- [1] Z. Xu, H. Sun, X. Zhao, C. Gao, *Adv. Mater.* **2013**, 25, 188.
- [2] X. Tang, H. Zhou, Z. Cai, D. Cheng, P. He, P. Xie, D. Zhang, T. Fan, *ACS Nano* **2018**, 12, 3502.
- [3] Y. Q. Jiang, Z. Xu, T. Q. Huang, Y. J. Liu, F. Guo, J. B. Xi, W. W. Gao, C. Gao, *Adv Funct Mater* **2018**, 28, 1707024.
- [4] X. W. Tang, C. L. Zhu, D. D. Cheng, H. Zhou, X. H. Liu, P. W. Xie, Q. B. Zhao, D. Zhang, T. X. Fan, *Adv Funct Mater* **2018**, 28, 1805057.

- 
- [5] D. X. Luong, A. K. Subramanian, G. A. L. Silva, J. Yoon, S. Cofer, K. Yang, P. S. Owuor, T. Wang, Z. Wang, J. Lou, P. M. Ajayan, J. M. Tour, *Adv Mater* **2018**, *30*, e1707416.
- [6] R. M. Hensleigh, H. Cui, J. S. Oakdale, J. C. Ye, P. G. Campbell, E. B. Duoss, C. M. Spadaccini, X. Zheng, M. A. Worsley, *Mater Horiz* **2018**, *5*, 1035.
- [7] Q. Zhang, F. Zhang, S. P. Medarametla, H. Li, C. Zhou, D. Lin, *Small* **2016**, *12*, 1702.
- [8] C. Zhu, T. Y. Han, E. B. Duoss, A. M. Golobic, J. D. Kuntz, C. M. Spadaccini, M. A. Worsley, *Nat. Commun.* **2015**, *6*, 6962.